

Electro-Optical Characterization of MWIR InAsSb Detectors

A.I. D'Souza^a, E. Robinson, A.C. Ionescu, D. Okerlund
DRS Sensors & Targeting Systems, 10600 Valley View Street, Cypress, CA 90630

T.J. de Lyon, H. Sharifi, M. Roebuck, D. Yap, R.D. Rajavel
HRL Laboratories, LLC, 3011 Malibu Canyon Rd., Malibu, CA 90265

N. Dhar
DARPA, MTO, 3701 N. Fairfax Dr., Arlington, VA 22203

P.S. Wijewarnasuriya
U.S. Army Research Laboratory, 2800 Powder Mill Road, Adelphi, MD 20783

C. Grein
University of Illinois at Chicago, 845 W. Taylor St., Chicago, IL, 60607

Abstract

InAs_{1-x}Sb_x material with an alloy composition of the absorber layer adjusted to achieve 200K cutoff wavelengths in the 5 μm range has been grown. Compound-barrier (CB) detectors were fabricated and tested for optical response and $J_{\text{dark}}-V_{\text{d}}$ measurements were acquired as a function of temperature. Based on absorption coefficient information in the literature and spectral response measurements of the midwave infrared (MWIR) nCBn detectors, an absorption coefficient formula $\alpha(E, x, T)$ is proposed. Since the presently suggested absorption coefficient is based on limited data, additional measurements of material and detectors with different x values and as a function of temperature should refine the absorption coefficient, providing a more accurate parametrization. Material electronic structures were computed using a $k \cdot p$ formalism. From the band structure, dark current density (J_{dark}) as a function of bias (V_{d}) and temperature (T) were calculated and matched to $J_{\text{dark}}-V_{\text{d}}$ at fixed T and $J_{\text{dark}}-T$ at constant V_{d} curves. There is a good match between simulation and data over a wide range of bias, but discrepancies that are not presently understood exist near zero bias.

a. e-mail: arvind.d'souza@drs-sts.com

Key Words : MWIR barrier detectors, photon trap structures

1.0 INTRODUCTION

The AWARE Broadband program requires an innovative detector architecture and processing techniques to achieve pioneering performance of MWIR detectors at 200 K. One of the ambitious requirements is to obtain high ($> 80\%$) quantum efficiency (QE) over the broad 0.5 to 5.0 μm spectral range while maintaining high D^* ($> 1.0 \times 10^{11} \text{ cm}^2 \sqrt{\text{Hz/W}}$) in the 3.0 to 5.0 μm spectral range. A prime method to accomplish these goals is by reducing the dark diffusion current in the detector via reducing the volume fill ratio (VFR) of the detector while optimizing absorption through the design of photon-trap topological structures in the absorber layer upon which the radiation is incident. For the program, InAsSb was chosen as the absorber layer of the multilayer compound barrier detector architecture.

MWIR photodetectors performance improvements were realized through the development of devices that rely upon bandgap engineering for the reduction of dark currents associated with depletion-region Shockley-Read-Hall (SRH) generation, surface current generation, and bulk diffusion. In particular, the nBn^{1,2} device in the InAsSb/AlAsSb materials system, is based on a simple design that utilizes a large conduction band barrier to suppress the flow of majority carrier electrons, thus eliminating the electric

field associated with a conventional p-n junction that results in high dark currents associated with depletion region generation-recombination currents. Thus, a properly designed nBn structure facilitates diffusion-dominated detector performance determined by the bulk minority carrier (hole) lifetime.

2.0 DETECTOR ARCHITECTURE

Innovative nBn barrier detectors^{1,2} were designed to suppress majority carrier currents while maintaining low electric fields. This nBn design was considered a remedy to the generation-recombination currents originating in the depletion region of p-n junction devices. AlAsSb alloy is used as a wide bandgap barrier material, due to having no significant valence band offset with respect to InAsSb, which facilitates the collection of minority carriers (holes) while providing a large barrier to majority carriers. However, the original InAsSb/AlAsSb barrier device design can have potential deficiencies associated with the choice of AlAsSb as the barrier material due to the alignment between the active layer and the barrier. Circumventing some of the difficulties resident in the original nBn design, a compound-barrier (CB) detector architecture³ was designed and implemented with the alloy composition of the InAsSb absorber layer adjusted to achieve a 200 K cutoff wavelength of 4.3 μm .^{4,5} The novel detector structure which is displayed in Figure 1, utilizes pyramid-shaped absorbers. Each detector pixel has an array of multiple pyramid-shaped absorbers. This detector structure provides the combination of reduced volume of absorber material, elimination of front-side reflection for incident light over a broad bandwidth, and enhanced photon trapping for high absorbance of incident light.

Infrared radiation is incident on the array of pyramids fabricated in the n-type InAsSb absorber which also serves as the array common or substrate contact. The detector array is hybridized via indium bumps to a Si fanout chip. The chip when inserted into an 84 pin leadless chip carrier (LCC) permits direct access to approximately 80 detectors. Detector areas ranged from $3.6 \times 10^{-5} \text{ cm}^2$ to $1.15 \times 10^{-3} \text{ cm}^2$. The common contact to the absorber layer is a remote contact and adjacent detectors were not biased during measurement of the reference detector.

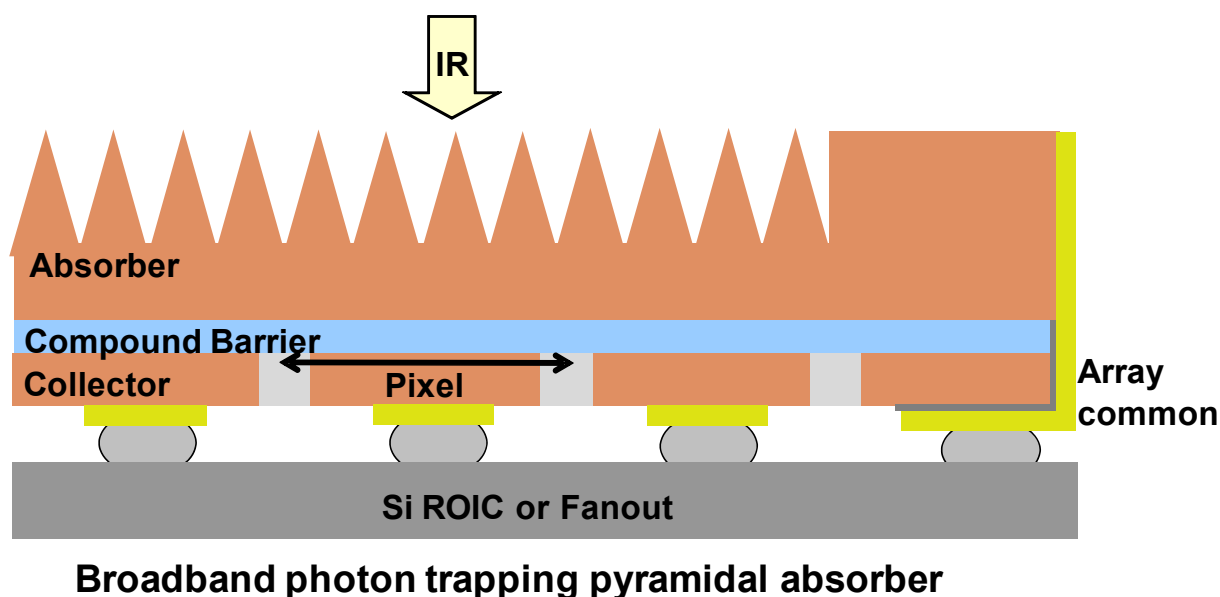


Figure 1. Compound barrier detector architecture with pyramid shaped absorber layer

3.0 MATERIAL and DETECTOR MODELING

Modeling InAs_{1-x}Sb_x -based device performance requires obtaining experimental and/or theoretical material parameters. InAs_{1-x}Sb_x is a ternary compound whose bandgap changes as a function of x and temperature T . Clear-cut experimental or theoretical information on InAs_{1-x}Sb_x(x, T) is sparse, therefore requiring the utilization of approximations that “best” fit the data or equations available, and then generalizing the model.

Bandgap $E_g(x, T)$ and cutoff wavelength λ_c

InAs_{1-x}Sb_x bandgap^{4,5} $E_g(x, T)$ in eV is given by Equation 1 and to a first approximation the cutoff wavelength is given by Equation 2. The cutoff wavelength as a function of x at a temperature $T = 200$ K is displayed in figure 2. The bandgap and cutoff wavelength at any other temperature can be calculated using Equations 1 and 2.

$$E_g(x, T) = 0.411 - \frac{3.4 \times 10^{-4} T^2}{210 + T} - 0.867x + 0.70x^2 + 3.4 \times 10^{-4} xT(1 - x) \quad --(1)$$

To a first approximation, cutoff wavelength λ_c in μm is,

$$\lambda_c(x, T) = \frac{1.2398}{E_g(x, T)} \quad --(2)$$

Using these expressions, $x \approx 0.21$ gives $\lambda_c = 5.25 \mu\text{m}$ at $T = 200$ K, .

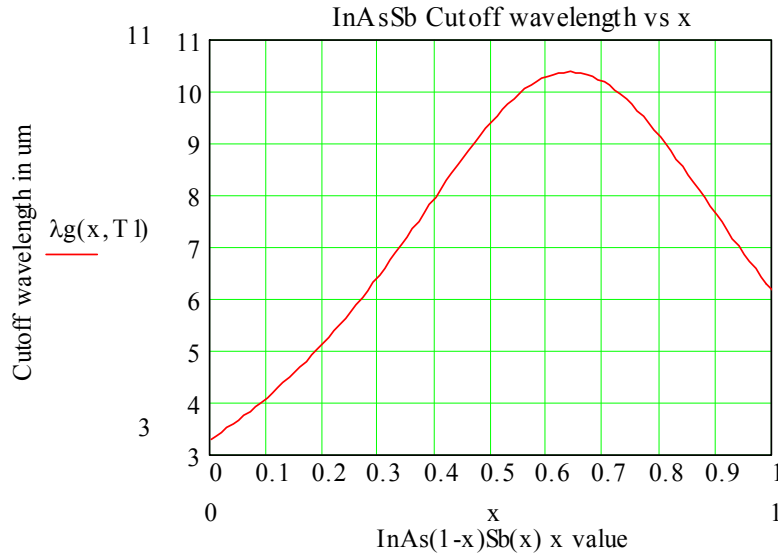


Figure 2. Variation in InAs_{1-x}Sb_x cutoff wavelength as a function of x at $T = 200$ K

Absorption Coefficient $\alpha(\lambda, x, T)$

Absorption coefficient information for InAs above the bandgap⁶ at room temperature and separately data for various x values for below bandgap photon energies⁷ is available in the literature. An empirical expression is suggested to best match the limited available data. Above the bandgap, the expression of

Moazzami et al⁸ was modified so that $\alpha(E_g)$ does not drop to zero but gives a value at the energy gap $\alpha(E_g) = 800 \text{ cm}^{-1}$. Energies below the bandgap utilize the Urbach tail⁹ expression. The constants in Equations 3a and 3b were picked to best replicate below-bandgap data in Reference 6. Above the bandgap, coefficients K and c in Equations 4a, 4b and 4c were picked to give values that attempted to match calculations made using the expression for InAs at $T = 300 \text{ K}$ found in Dixon and Ellis⁶. Shown in Figure 3 is the absorption coefficient $\alpha(\lambda, x = 0, T = 300\text{K})$, i.e. for InAs at $T = 300 \text{ K}$. Using Equations 3 and 4 permits one to calculate the absorption coefficient as a function of wavelength, x and T as shown in Figure 4 for $x = 0.19$ and $T = 200 \text{ K}$, i.e. for $\lambda \sim 5.05 \mu\text{m}$ at 200 K . The constants used in Equations 3 and 4 are not unique and will require refining as more absorption coefficient and spectral response data is acquired or becomes available. This section attempted to collate material properties from several sources and an equation for the absorption coefficient was developed to best match the available data. The absorption coefficient in Equations 3 and 4 will be utilized to calculate the absorption coefficient vs. wavelength for a MWIR $\text{InAs}_{0.81}\text{Sb}_{0.19}$ -based detector at 200 K . Further investigation into the spectral response of $\text{InAs}_{1-x}\text{Sb}_x$ detectors will test the utility of the following absorption coefficient expressions.

For photon energies $E \leq E_g$,

$$\alpha(E, x, T) = 948.23 \times e^{170(E-E_0)} \quad \text{--(3a, b)}$$

$$E_0 = E_g + 0.001$$

For photon energies $E > E_g$,

$$\alpha(E, x, T) = \frac{[K(E - E_g - c)\sqrt{(E - E_g - c)^2 - c^2}]}{E} + 800$$

$$c = 0.5E_g + 0.1 \quad \text{--(4a-c)}$$

$$K = 10000 + 20000E_g$$

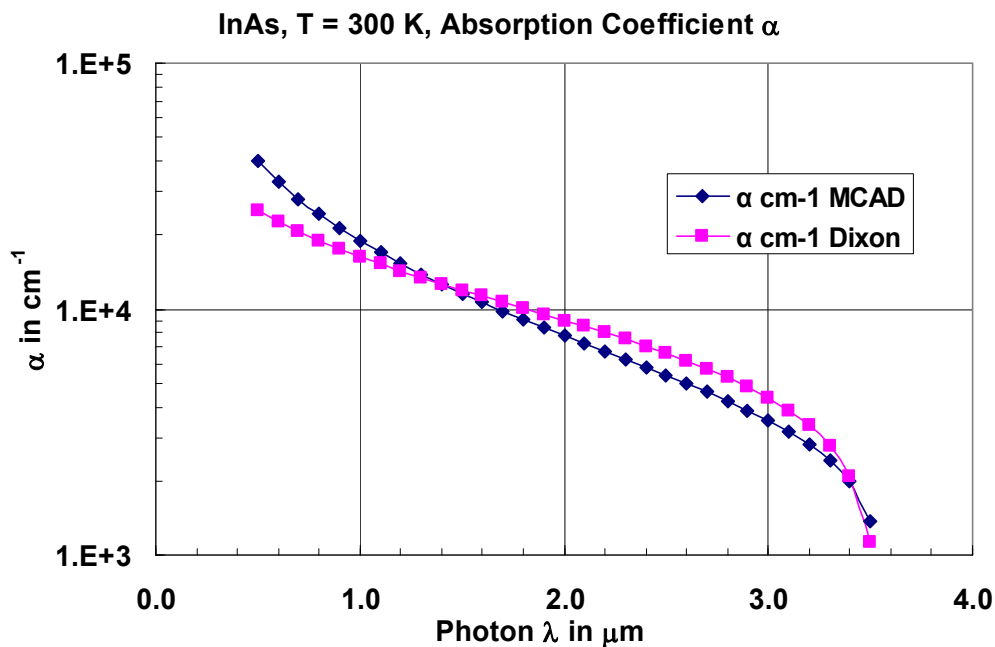


Figure 3. Match between $\alpha(\lambda, x = 0, T = 300 \text{ K})$ from the literature (“Dixon”)⁵ and calculated using Equations 3a, 3b, 4a, 4b and 4c (“MCAD”). MCAD is a software package (Mathcad) marketed by MathSoft Engineering & Education, Inc. (Cambridge, MA). The user defines a set of operations that Mathcad uses to perform engineering calculations.

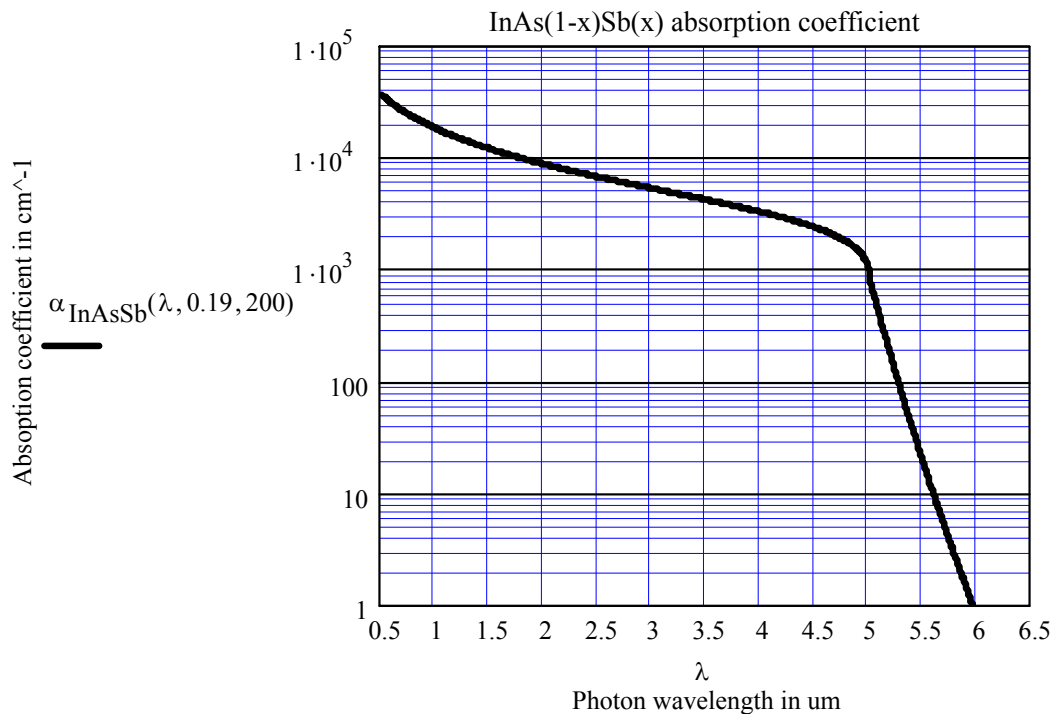


Figure 4. $\text{InAs}_{0.81}\text{Sb}_{0.19}$ absorption coefficient versus wavelength at $T = 200 \text{ K}$ using Equations 3 and 4

Band Structure

The material electronic structures were computed with a $\mathbf{k} \cdot \mathbf{p}$ formalism¹⁰. The zone-center states are calculated in Fourier space using a 14-band basis. The need to rely on a 14-band basis rather than the more common 8-band basis arises because of the sensitivity of the optical and electronic properties to the electronic structure in the secondary regions of the band structure. Errors inherent in the 8-band model become significantly more pronounced as the states one is interested in become farther from the band edge^{10,11}. Results of the $\text{InAs}_{1-x}\text{Sb}_x$ electronic structure calculations for $x = 0.19$ at $T = 200$ K are displayed as a band structure plot in Figure 5.

Figures 6a and 6b, 7a and 7b are the conduction and valence bands through the nCBn detector at bias values $V_d = -0.2, -0.4, -1.4$ and -3.0 V respectively. The n-type $\text{InAs}_{1-x}\text{Sb}_x$ absorber region, which may be a ~ 5 μm thick layer or a thin layer contoured with pyramids are at the left of Figures 6a, 6g, 7a and 7b. In all references through this paper, the bias sign convention is the bias applied to the n+ contact region. In other words, a bias listed as $V_d = -0.4$ V implies a bias of -0.4 V is applied to the n+ contact layer while the n-type absorber layer is held at zero bias or conversely the n+ contact layer is held at zero bias while a $+0.4$ V bias is applied to the n-type absorber layer. As can be seen from Figure 6a, there is still a ~ 100 meV valence band barrier when $V_d = -0.2$ V is applied to the n+ contact layer. Therefore, it should be expected that the QE will be low at $V_d = -0.2$ V. At $V_d = -0.4$ V, the valence band barrier is virtually non-existent and the QE should be high. At $V_d = -1.4$ V and -3.0 V, there is no valence band barrier (Figures 7a and 7b), resulting in photo generated holes having unimpeded flow to the n+ contact, which has the potential for high QE. However, the dark current can increase substantially at $V_d = -3.0$ V from tunneling currents which result in a lowering of QE.

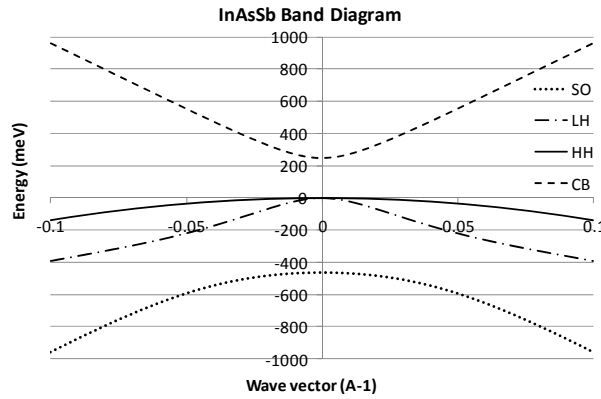


Figure 5. Computed band structure diagram for $\text{InAs}_{1-x}\text{Sb}_x$ with $x = 0.19$ at $T = 200$ K

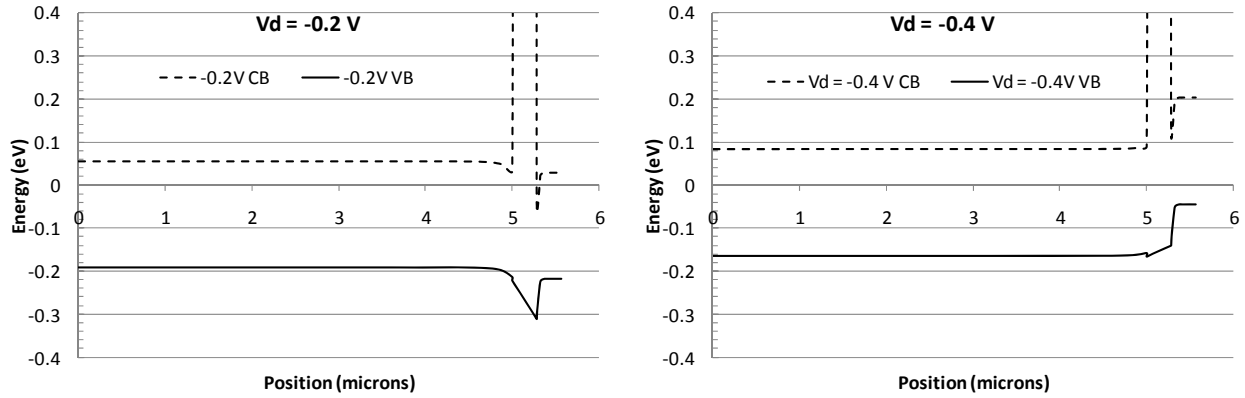


Figure 6. Computed conduction (CB) and valence (VB) bands at a) $V_d = -0.2$ and b) $V_d = -0.4$ V through the nCBn detector

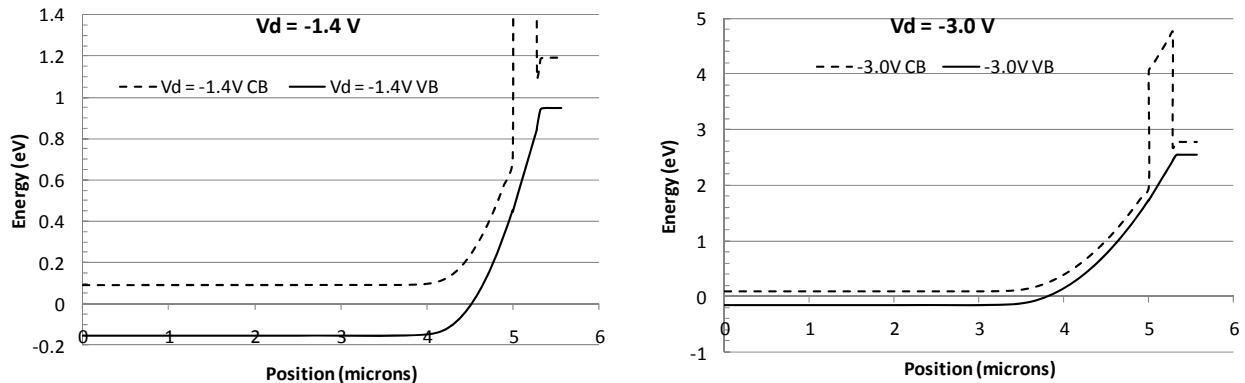


Figure 7. Computed conduction (CB) and valence (VB) bands at a) $V_d = -1.4$ and b) $V_d = -3.0$ V through the nCBn detector

4.0 OPTICAL DATA and ANALYSIS

$\text{InAs}_{1-x}\text{Sb}_x$ with a bandgap corresponding to a cutoff wavelength of $5.05 \mu\text{m}$ at 200 K was grown on a GaAs substrate. The measured devices had the carrier wafer removed, providing the opportunity to measure detectors with the incident radiation impinging directly on the pyramid array. Knowledge of the blackbody temperature, transmission of a narrow band filter, window transmission, dewar geometry and distances of the blackbody from the detector were utilized to calculate the flux incident on the detector. The photocurrent density J_{photo} as a function of bias V_d was measured at blackbody temperature settings of 400 K and 450 K, the difference between the two providing the data for the calculation of the QE vs wavelength plot shown in Figure 8. There is no multilayer AR-coating since the pyramids perform the AR-coating function. The QE attains its maximum value of 0.82 at -1.5 V bias. As the bias increases beyond -1.5 V, the QE starts to fall since the detector tends to be increasingly dominated by tunneling currents. It is presently unclear as to what energy barriers are present that result in requiring a -1.5 V bias to attain peak QE. Shown in Figure 9 is a QE vs wavelength “Data” curve for the same detector as shown in Figure 8. Measurements were made using a Fourier transform infrared (FTIR) spectrometer and the QE is seen to be high across the entire 2.0 to $4.6 \mu\text{m}$ band. Measurements still need to be made in the visible wavelength region.

The bandgap from Equation 1 and the absorption coefficient from Equations 3 and 4 are used to calculate the QE versus wavelength curve listed as “Model” in Figure 9. An x value of 0.19 which results in a bandgap $E_g = 247.1$ meV was chosen for the “Model” curve. Since the detector has pyramids that minimize the reflectance and maximize absorption in the $\text{InAs}_{1-x}\text{Sb}_x$ material, reflectance in the model was set at 0.05 and the effective thickness of the absorber layer was set at $7\text{ }\mu\text{m}$. The experimental QE falls toward zero much faster than the “Model” in the 5.4 to $5.8\text{ }\mu\text{m}$ range. One reason could be that the absorption coefficient in that range is higher than that obtained from Equation 3. Another potential explanation is that the pyramid photon trap structures absorption is higher than that modeled by a $7\text{ }\mu\text{m}$ thick effective absorber. There are too many fitting parameters in the absorption coefficient equation to conclude that the absorption coefficient from Equations 3 and 4 is the absorption coefficient of $\text{InAs}_{1-x}\text{Sb}_x$. It serves as a starting point for determining the absorption coefficient, which can be adjusted based on additional measurements made by varying the temperature and x value of $\text{InAs}_{1-x}\text{Sb}_x$ material.

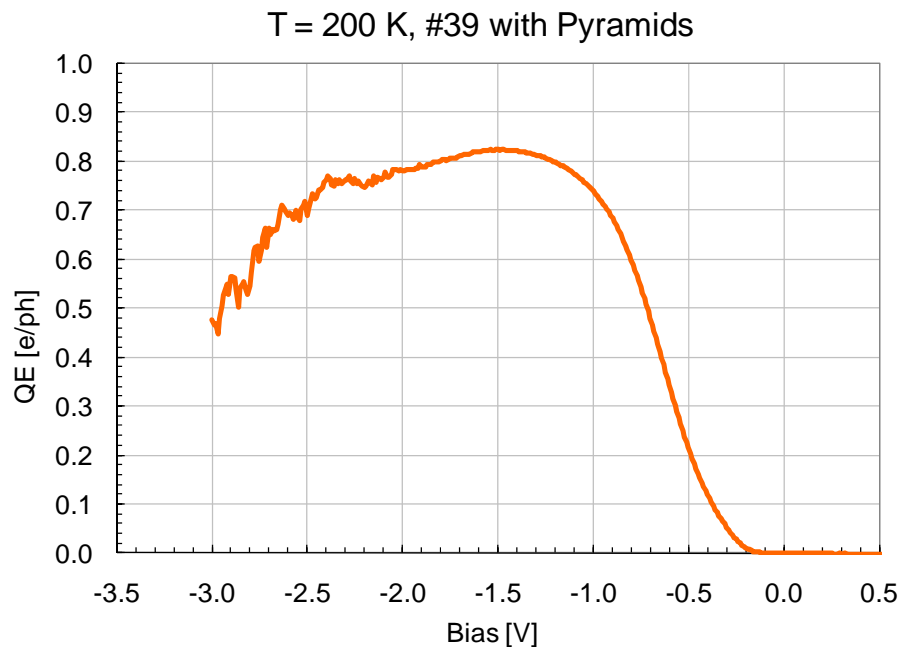


Figure 8. QE vs V_d data calculated from $J_{\text{photo}} - V_d$ curves

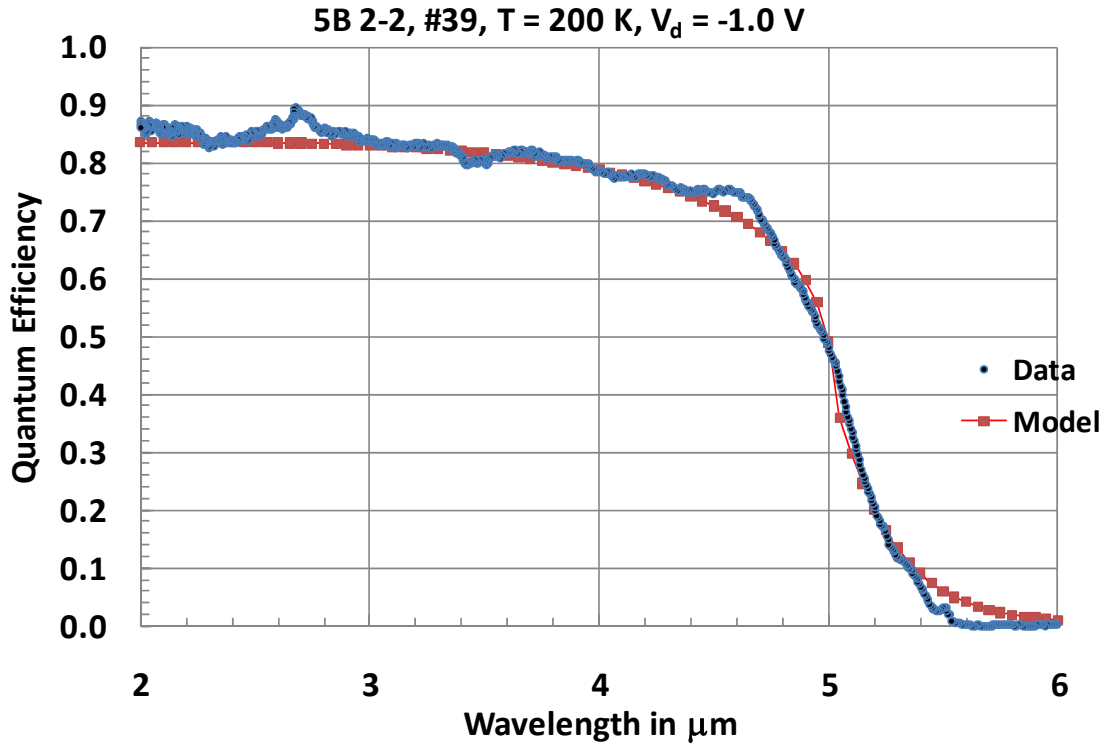


Figure 9. QE vs wavelength model and data at 200 K and $V_d = -1.0$ V

5.0 ELECTRICAL MODELING, DATA and ANALYSIS

Modeling

Device transport was modeled employing a standard formalism¹⁴. The principal equations are reproduced here to clarify which physical generation/recombination mechanisms are considered, how they are treated, and introduce parameters that appear in Table I. Poisson's equation (5) and the two current continuity equations (6, 7) were solved self-consistently and with Fermi statistics under steady-state conditions to simulate device transport.

$$\nabla \cdot \mathbf{D}(x) - \rho(x) = 0 \quad (5)$$

$$\nabla \cdot (\mathbf{J}_n(x)/q) - U_{\text{tot}}(x) = 0 \quad (6)$$

$$\nabla \cdot (\mathbf{J}_p(x)/q) + U_{\text{tot}}(x) = 0 \quad (7)$$

where \mathbf{D} is the electrostatic displacement, and $\mathbf{J}_n, \mathbf{J}_p$ are the electron and hole current densities, respectively.

The total generation/recombination rate is

$$U_{\text{tot}} = U_{\text{SRH}} + U_{\text{rad}} + U_{\text{Auger}} - G_{\text{BBT}} \quad (8)$$

where the Shockley-Read-Hall rate is given by

$$U_{\text{SRH}} = (np - n_i^2) / ((p + n_i) \tau_{n0} + (n + n_i) \tau_{p0}) \quad (9)$$

the radiative rate is given by

$$U_{\text{rad}} = B(np - n_i^2) \quad (10)$$

the Auger rate by

$$U_{\text{Auger}} = (np - n_i^2)(nC_n + pC_p) \quad (11)$$

and the band to band tunneling rate is

$$G_{\text{BBT}} = A_t E^{\text{Bt}} \exp(-C/E), \quad (12)$$

where n , p are the electron, hole concentrations, n_i is the intrinsic carrier concentration, τ_{n0} and τ_{p0} are the electron and hole SRH lifetimes, B is the radiative coefficient, C_n and C_p are the electron and hole Auger coefficients, and E is the electric field.

Data and Analysis

The dark current density J_{dark} was measured as a function of bias V_d for a number of detectors as a function of temperature between 140 K and 220 K. In order to minimize operator intervention, a semiconductor parameter analyzer in conjunction with a switching matrix is used to acquire current as a function of bias for multiple detectors in sequence at each temperature. Figure 10 plots J_{dark} vs V_d for one of the detectors, #39. A switching matrix is used to acquire data for a multitude of detectors sequentially, reducing time and tedium for the involved experimenter. However, a switching matrix introduces noise that is evident in the $J_{\text{dark}} - V_d$ curve at 140 K. The dark current density J_{dark} at $V_d = -1.5$ V is plotted vs. $1000/T$ in Figure 11 to extract the activation energy at the bias at which QE attained its maximum value. From Figure 11, the activation energy $E_a = 275.9$ meV is extracted which is close to the bandgap $E_g(x = 0.19, T = 0 \text{ K}) = 269.8$ meV, suggesting that the dominant dark current at $V_d = -1.5$ V is a diffusion current.

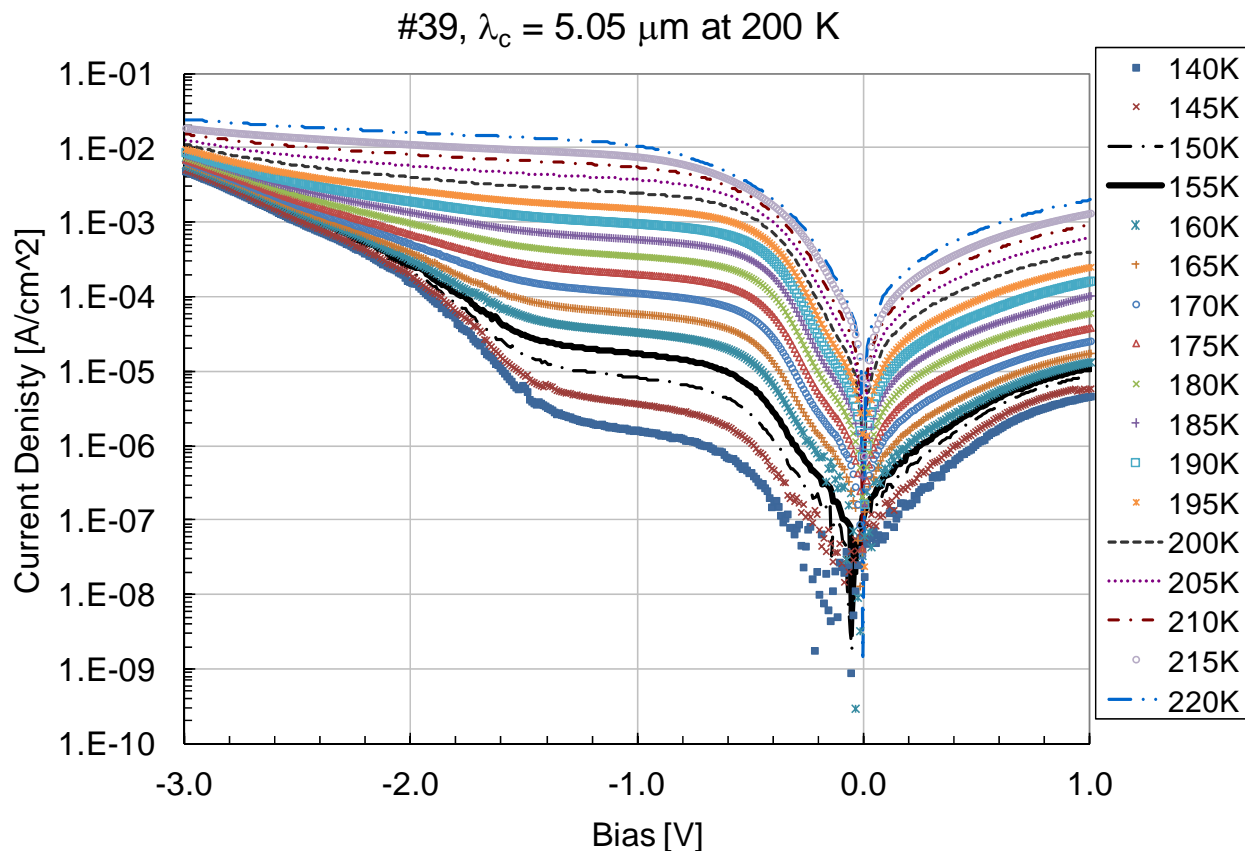


Figure 10. Dark current density $J_{\text{dark}} - V_d$ curves as a function of temperature for an nCBn $5.05 \mu\text{m}$ at 200 K $\text{InAs}_{1-x}\text{Sb}_x$ photon trap structure detector

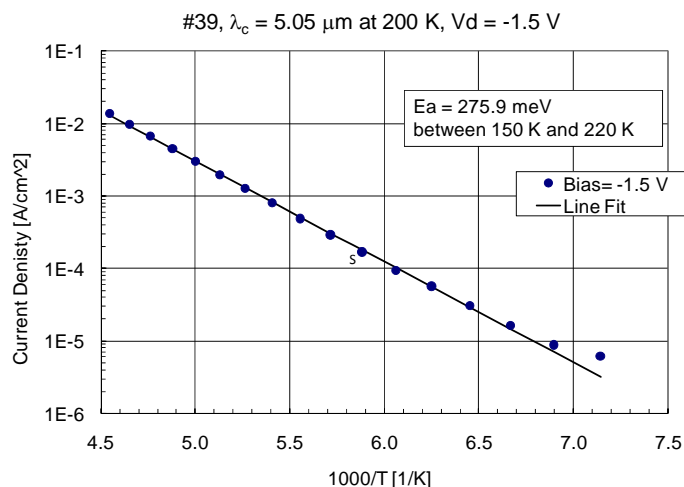


Figure 11. Dark current density $J_{\text{dark}} - T$ at $V_d = -1.5 \text{ V}$ provides activation energy $E_a = 275.9 \text{ meV}$

Figure 12a compares device transport simulations to experimental J_{dark} vs temperature at $V_d = -1.5 \text{ V}$. There is good agreement at the higher temperatures with some deviation as the temperature is decreased, the experimental values of J_{dark} being lower than the simulated values. Figure 12b is a plot of the simulated and experimental $J_{\text{dark}} - V_d$ at $T = 200 \text{ K}$. The fit is good at large bias values, however the experimental values deviate from the simulation at reverse bias values less than $\sim 0.5 \text{ V}$. Lower experimental J_{dark} as compared to simulation in the $\sim 0.2 \text{ V}$ to 0.5 V reverse bias range is probably caused

by the same barrier that limits the QE from not attaining a maximum value until the bias is -1.5 V. Table I specifies the input parameters employed to compute dark current density $J_{\text{dark}} - V_d$ curve at 200 K. The properties (including the conduction electron and heavy hole effective masses m_c and m_{hh} , respectively, relative to the free electron mass m_0) were obtained from the cited sources. The last four columns are fitted parameters to reproduce the $J_{\text{dark}} - V_d$ for detector #39. Zero values specify quantities that are not expected to affect results. Figures 13a, 13b, 14a and 14b are plots of dark current density J_{dark} vs $1000/T$ that are used to extract the activation energy at -0.2 V, -0.4 V, -1.4 V and -3.0 V respectively. The activation energy E_a ($V_d = -0.2$ V) = 331.9 meV is close to the bandgap energy and valence band barrier of 356 meV (see Figure 6a). However, at $V_d = -0.4$ V, there is virtually no valence band barrier (see Figure 6b), so it is not understood as to the reason for the activation energy E_a ($V_d = -0.4$ V) = 342.7 meV (Figure 13b). As expected from the dominance of diffusion current at $V_d = -1.4$ V, E_a ($V_d = -1.4$ V) = 278.9 meV is close to the bandgap energy, $E_g(x = 0.19, T = 0 \text{ K}) = 269.8 \text{ meV}$. At $V_d = -3.0$ V, the dark current density has minimal temperature dependence, a characteristic of tunneling currents, a consequence of the conduction and valence band lineup seen in Figure 7b.

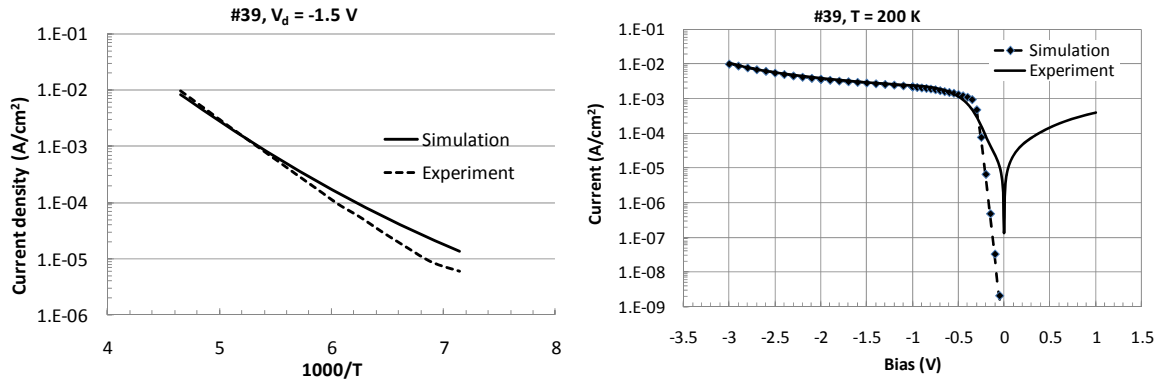


Figure 12. Simulated and measured a) dark current density J_{dark} vs temperature at $V_d = -1.5$ V and b) $J_{\text{dark}} - V_d$ curve at $T = 200$ K for $N_d = 1.0 \times 10^{15} \text{ cm}^{-3}$

Table I. Detector component layer material parameter and fitting parameters for $J_{\text{dark}} - V_d$ curve at 200 K

Material	m_c/m_0 (Ref 12)	m_{hh}/m_0 (Ref 12)	B (cm^3/s) (Ref 13)	C_n (cm^6/s) (Ref 13)	C_p	τ_{n0}	τ_{p0} (s)	A_t ($\text{V}^2\text{s cm}$) ⁻¹	B_t	C_t (V/cm)
InAs _{0.81} Sb _{0.19}	0.015	0.37	9.9×10^{-11}	9×10^{-27}	0	5×10^{-5}	5×10^{-7}	1.2×10^{15}	1.9	1.0×10^6
Compound Barrier	0.13	0.43	0	0	0	5×10^{-5}	5×10^{-7}	0	0	0

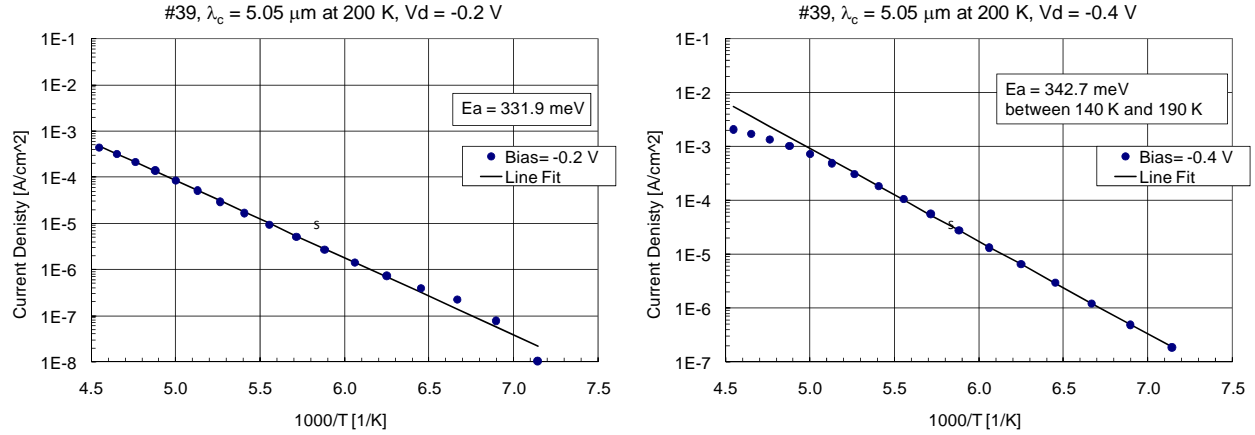


Figure 13. Dark current density $J_{\text{dark}} - T$ at a) $V_d = -0.2$ V and b) $V_d = -0.4$ V to determine activation energy

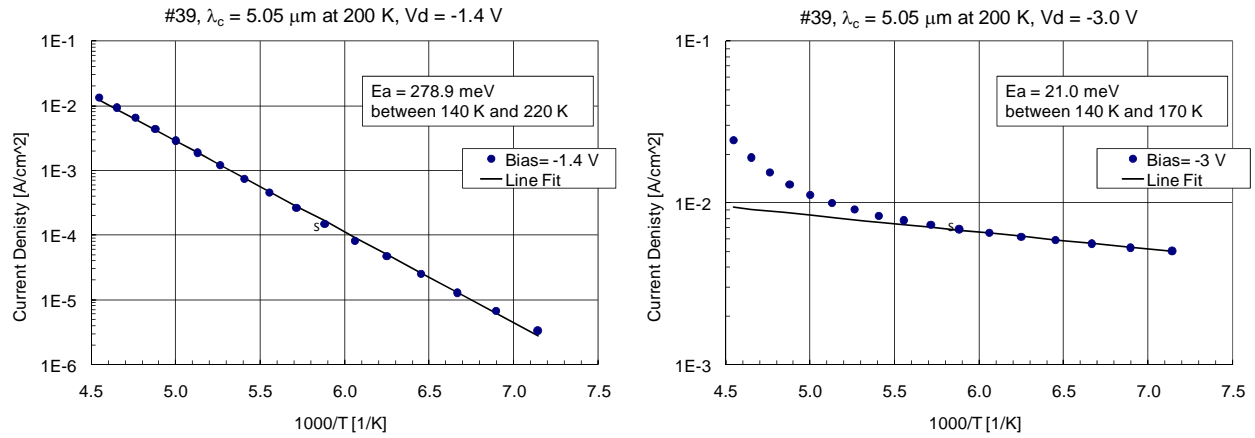


Figure 14. Dark current density $J_{\text{dark}} - T$ at a) $V_d = -1.4$ V and b) $V_d = -3.0$ V to determine activation energy

6.0 CONCLUSIONS

InAs_{1-x}Sb_x nCBn detectors with cutoff wavelengths in the 5 μm range at 200 K were fabricated and characterized for optical properties and electrical performance as a function of temperature. Absorption coefficient information from the literature and spectral response measurements of the MWIR nCBn detectors were combined to propose an absorption coefficient $\alpha(E, x, T)$ model. Additional measurements of material and detectors with different x values and as a function of temperature are needed to provide a more accurate value of the absorption coefficient. Band structures were computed using a $k \cdot p$ formalism and from the band structure, the dark current density as a function of bias and temperature was simulated and compared to $J_{\text{dark}} - V_d$ at fixed T and $J_{\text{dark}} - T$ at constant V_d curves. There is a good match between simulation and data over a wide range of bias, but between -0.4 V and zero bias, simulations and experiment diverge. Activation energy for the dark current was extracted at various biases using the $J_{\text{dark}} - V_d$ measurements with temperature as a parameter. The dark current activation energy E_a at $V_d = -0.2$ V seems to be a function of the bandgap plus a valence band barrier. At $V_d = -0.4$ V, the high E_a is not yet understood. E_a is approximately equal to the bandgap in the -1.4 to -1.5 V range where the dominant dark current is a diffusion current and the QE is high. Tunneling dominates the dark current at $V_d = -3.0$ V as expected from the band profile and confirmed by the low activation energy value.

7.0 ACKNOWLEDGEMENTS

This work was supported by DARPA under contract N66604-09-C-3652 (Dr. Nibir Dhar, DARPA Program Manager). However, **“The views expressed are those of the author and do not reflect the official policy or position of the Department of Defense or the U.S. Government.” This is in accordance with DoDI 5230.29, January 8, 2009.**

Special thanks to Mr. Dan Okerlund, the ever patient Program Manager at DRS, Dr. Ravi Dat, Booz Allen Hamilton for technical and other advice, and Ms. Yesim Anter for helping prepare the manuscript. Excellent work was performed by Prof. Saif Islam and his team at UC Davis who were instrumental in different aspects of the processing sequence.

8.0 REFERENCES

1. S. Maimon and G.W. Wicks, APL 89, 151109 (2006).
2. White, Anthony M., USA Patent No. 4,679,063 (1987).
3. A. I. D'Souza, A. C. Ionescu, M. Salcido, E. Robinson, L.C. Dawson, D. L. Okerlund, T.J. de Lyon, R. D. Rajavel, H. Sharifi, D. Yap, M.L. Beliciu, S. Mehta, W. Dai, G. Chen, N. Dhar, P. Wijewarnasuriya, SPIE Vol. 8012, Defense & Security, Orlando, FL., 25-29 April, 2011.
4. H.H. Wieder, A.R. Clawson, Thin Solid Films, 15, 217 (1973).
5. A. Rogalski, Prog. Quant. Electr. 13, 191 (1989).
6. J.R. Dixon, J.M. Ellis, Phys. Rev. 123, 1560 (1971).
7. G.B.Stringfellow, P.E.Greene, J. Electrochem.Soc., 118, no.5, 805 (1971).
8. K. Moazzami, J. Phillips, D. Lee, S. Krishnamurthy, G. Benoit, Y. Fink, T. Tiwald, J. Elect. Mater. 34, 773 (2005).
9. F. Urbach, Phys. Rev. 92, 1324 (1953).
10. J.T. Olesberg, Ph.D. Thesis, University of Iowa, 1999.
11. C. W. Cheah, L. S. Tan, and G. Karunasiri, J. Appl. Phys. **91**, 5105 (2002)
12. Computed from 14 band k.p electronic structure.
13. <http://www.ioffe.ru/SVA/NSM/Semicond/> with Vegard's Law applied
14. See for example C.M. Snowden, "Semiconductor device modeling", Springer-Verlag, 1989 - Technology & Engineering